

# Spontaneous Dynamical Disordering of Borophenes in MgB<sub>2</sub> and Related Metal Borides

**Sichi Li**

Lawrence Livermore National Laboratory <https://orcid.org/0000-0002-2565-5906>

**Harini Gunda**

India Institute of Technology, Gandhinaga

**Keith Ray**

Lawrence Livermore National Laboratory

**Chun-Shang Wong**

Sandia National Laboratories

**Penghao Xiao**

Lawrence Livermore National Laboratory <https://orcid.org/0000-0002-5846-6343>

**Raymond Friddle**

Sandia National Laboratories California <https://orcid.org/0000-0003-1201-8745>

**Yi-Sheng Liu**

Lawrence Berkeley National Laboratory <https://orcid.org/0000-0002-1085-1947>

**ShinYoung Kang**

Lawrence Livermore National Laboratory

**Joshua Sugar**

Sandia National Laboratories

**Robert Kolasinski**

Sandia National Laboratories

**Liwen Wan**

Lawrence Berkeley National Laboratory

**Alexander Baker**

Lawrence Livermore National Laboratory

**Jonathan Lee**

Lawrence Livermore National Laboratory <https://orcid.org/0000-0001-7316-7643>

**Kabeer Jasuja**

Indian Institute of Technology <https://orcid.org/0000-0002-4332-0712>

**Mark Allendorf**

Sandia National Laboratories <https://orcid.org/0000-0001-5645-8246>

**Vitalie Stavila**

Sandia National Laboratories <https://orcid.org/0000-0003-0981-0432>

**Brandon Wood** (✉ [brandonwood@llnl.gov](mailto:brandonwood@llnl.gov))

## Article

**Keywords:** metal diborides, borophenes, dynamic surface, surface disordering, 17 hydrogen storage

**Posted Date:** May 19th, 2021

**DOI:** <https://doi.org/10.21203/rs.3.rs-531927/v1>

**License:**   This work is licensed under a Creative Commons Attribution 4.0 International License.

[Read Full License](#)

---

**Version of Record:** A version of this preprint was published at Nature Communications on November 1st, 2021. See the published version at <https://doi.org/10.1038/s41467-021-26512-4>.

# Spontaneous Dynamical Disordering of Borophenes in $\text{MgB}_2$ and Related Metal Borides

Sichi Li,<sup>\*,†</sup> Harini Gunda,<sup>‡,¶</sup> Keith G. Ray,<sup>†</sup> Chun-Shang Wong,<sup>‡</sup> Penghao Xiao,<sup>†</sup>  
Raymond W. Friddle,<sup>‡</sup> Yi-Sheng Liu,<sup>§</sup> ShinYoung Kang,<sup>†</sup> Joshua D. Sugar,<sup>‡</sup>  
Robert D. Kolasinski,<sup>‡</sup> Liwen F. Wan,<sup>†</sup> Alexander Baker,<sup>†</sup> Jon Lee,<sup>†</sup> Kabeer  
Jasuja,<sup>¶</sup> Mark D. Allendorf,<sup>‡</sup> Vitalie Stavila,<sup>\*,‡</sup> and Brandon C. Wood<sup>\*,†</sup>

<sup>†</sup>*Materials Science Division, Quantum Simulation Group, Lawrence Livermore National  
Laboratory, Livermore, CA 94550, United States*

<sup>‡</sup>*Sandia National Laboratories, Livermore, CA 94551, United States*

<sup>¶</sup>*Department of Chemical Engineering, Indian Institute of Technology Gandhinagar,  
Gujarat 382355, India*

<sup>§</sup>*The Advanced Light Source, Lawrence Berkeley National Laboratory, Berkeley, CA  
94720, United States*

E-mail: li77@llnl.gov; vnstavi@sandia.gov; brandonwood@llnl.gov

## Abstract

Layered boron compounds have attracted significant interest in applications from energy storage to electronic materials to device applications, owing in part to a diversity of surface properties tied to specific arrangements of boron atoms. Here, first-principles calculations coupled with global optimization are performed to explore the energy landscape for surface atomic configurations of  $\text{MgB}_2$ , a prototypical layered metal diboride. We demonstrate, that contrary to previous assumptions, multiple reconstructions are thermodynamically preferred and kinetically accessible within the exposed B surfaces in  $\text{MgB}_2$ , and other layered metal diborides. Such a dynamic environment and intrinsic disordering of the B surface atoms in metal borides presents new opportunities to realize a diverse set of 2D boron structures. We validated the predicted dynamic surface disordering by characterizing exfoliated boron-terminated  $\text{MgB}_2$  nanosheets. Application-relevant implications are discussed, with a particular view towards understanding the impact of boron surface heterogeneity on hydrogen storage performance.

**Keywords:** metal diborides, borophenes, dynamic surface, surface disordering, hydrogen storage

# 1 Introduction

Materials containing two-dimensional boron sheets, including metal diborides ( $\text{MB}_2$ ) and closely related borophene sheets, represent a rich and diverse class of materials with a potentially high degree of structural and electronic tunability.<sup>1,2</sup> As such, they have attracted interest in a wide variety of applications, including hydrogen storage,<sup>3</sup> superconductivity,<sup>4</sup> electrocatalysis,<sup>5-10</sup> optoelectronics,<sup>11</sup> and thermal<sup>12,13</sup> and corrosion resistance.<sup>14</sup> In several of these applications, the specific  $\text{MB}_2$  surface properties play an outsized role in determining the overall behavior, for example their surface-dependent electrocatalytic functions.<sup>15</sup> Recognizing this fact, several recent theoretical studies documented a library of possible two-dimensional boron sheets with differing surface stoichiometries and atomic arrangements generally derived from the parent P6/mmm structure of  $\text{MgB}_2$  which has a graphitic arrangement of boron atoms.<sup>16-18</sup>

Such studies highlight the importance of accurately assessing the surface structure of layered borides and borophenes, which is necessary for reliable predictions of surface-relevant properties. High-resolution ex situ imaging of boron surface structures in these materials is extremely challenging due to the low surface population of clean basal boron planes, which have relatively high surface energies<sup>19-22</sup> and are susceptible to contamination from surface oxidation.<sup>23,24</sup> Nevertheless, there is reason to believe that clean boron surfaces are manifested, particularly when boron surfaces are formed under *in situ* conditions. For instance, Li *et al.* confirmed a loss of oxidized borate signal from X-ray photoemission spectroscopy of  $\text{FeB}_2$  following surface hydrogen evolution, suggesting Fe surfaces are leached by the electrolyte under reaction conditions to expose the boron surface underneath.<sup>25</sup> Under such conditions, however, surface structure cannot be straightforwardly assessed. In particular, although it is undisputed that planar boron sheets exhibit graphitic patterns of extended hexagonal rings inside bulk crystals of metal diborides, it is an open question whether these same patterns are always preserved for boron on external surfaces. In addition to complicat-

44 ing the construction of reliable surface models, this knowledge gap jeopardizes understanding  
45 of how such boron surfaces behave under application-relevant conditions.

46 There have been some computational studies hinting at potential boron surface recon-  
47 struction in layered metal borides. Suehara *et al.* observed from ab initio molecular dynam-  
48 ics (AIMD) that the stoichiometric B-terminated (0001) surface of  $\text{ZrB}_2$ , when annealed,  
49 exhibited boron aggregation and formation of umbrella-like  $\text{B}_7$  clusters, suggesting the ex-  
50 istence of competing stable surface patterns.<sup>16</sup> Similarly, based on AIMD simulations, Kim  
51 *et al.* predicted that the B surface of  $\text{MgB}_2$  rapidly reconstructs upon adsorption of oxygen  
52 at 600 K, eliminating the  $E_{2g}$  phonon mode coupling to the in-plane electronic states and  
53 disabling the high-Tc superconductivity.<sup>26</sup> Reconstruction has also been reported for other  
54 two-dimensional boron systems. For instance, Liu *et al.* found by density functional theory  
55 (DFT) calculations that a free-standing boron sheet with an equivalent B density as  $\text{MB}_2$   
56 abandons the hexagonal lattice and undergoes self-amorphization via small perturbations  
57 in its initial structure.<sup>18</sup> This same behavior was observed for a borophene layer coated on  
58 silver substrates. Collectively, these studies suggest that the expected extended hexagonal  
59 pattern in certain exposed 2D boron sheets may not always be favored depending on the  
60 nature of the substrate.

61 In this work, we revisit the question of surface boron structure by combining DFT cal-  
62 culations with an exhaustive global optimization approach and free energy sampling, as well  
63 as synthesis and characterization of boron-terminated  $\text{MgB}_2$  nanosheets, thereby providing  
64 a comprehensive energy landscape and experimental validation for surface reconfiguration.  
65 Using  $\text{MgB}_2$  as a model metal diboride, we explore the complex interplay between sur-  
66 face electronic structure and atomic rearrangement to show that, contrary to conventional  
67 assumptions, exposed boron surfaces spontaneously and dynamically disorder. Additional  
68 electronic structure analysis reveals that the disordering tendency can be attributed to partial  
69 charge transfer at the undercoordinated surface, which leads to a frustrated, elemental-like  
70 boron state. This predicted disordering is confirmed using a combination of surface-sensitive

71 characterization techniques applied to synthesized  $\text{MgB}_2$  nanosheets. To illustrate the im-  
72 plications of the surface disordering, we focus on the technological application of  $\text{MgB}_2$  for  
73 hydrogen storage, showing how the introduction of heterogeneity impacts hydrogenation  
74 thermodynamics and kinetics. We then apply our insights to define design rules for delib-  
75 erately prohibiting or creating boron surface disorder by surveying a diverse set of layered  
76 metal diborides, thereby enhancing understanding of boron surface chemistry and expanding  
77 the library of possible 2D boron structures.

## 78 2 Results

### 79 2.1 Prediction of $\text{MgB}_2$ surface disordering

80 We begin with a discussion on the possible ways in which the surface B atoms can rearrange  
81 within the B plane in  $\text{MgB}_2$  (shown in **Figure 1**). Starting with an unreconstructed  $2 \times 2$   
82 B-terminated (0001) surface model with the expected hexagonal pattern of surface B atoms  
83 ( $B_{\text{surface}}$ ), we first relaxed the geometry to confirm that this structure can be classified as  
84 a metastable local minimum. Next, to initiate the search for other local-minimum surface  
85 patterns, we enumerated possible  $B_{\text{surface}}$  locations on either bridge or hollow sites, ultimately  
86 obtaining 135 possible initial patterns for the  $2 \times 2$  surface model. These structures were then  
87 relaxed to in total 16 unique local minima. (A detailed schematic of model construction  
88 and surface structures of all local minima can be found in the Supporting Information (SI)  
89 Section 1). Attempts to similarly distort subsurface boron atoms had no effect, as they  
90 relaxed back to the same hexagonal pattern, thus confirming that the new local minima are  
91 found in the surface layer only.

92 Figure 1 reports the DFT-computed energies of the local-minimum surface structures  
93 (blue circles), referenced to the unreconstructed hexagonal surface pattern. The values are  
94 plotted against the average B-B coordination number of ( $B_{\text{surface}}$ ), defined within a cutoff  
95 distance of  $2 \text{ \AA}$  and averaged over all  $B_{\text{surface}}$ . It is immediately apparent that patterns with

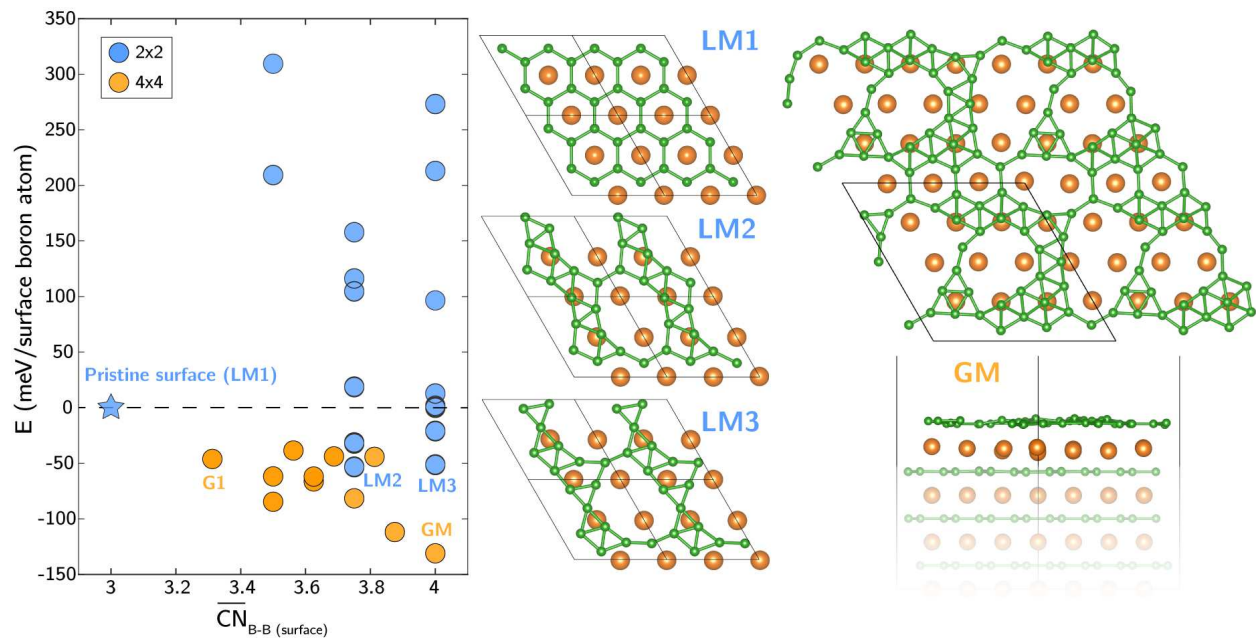


Figure 1: **Reconstruction of boron sheets.** Energy of 2x2 (blue) and 4x4 (orange) slabs with different locally stable surface patterns found during the structure search, referenced to the pristine hexagonal surface (blue star) and plotted against the average surface B-B coordination number. Select surface structures of interest are labeled, with corresponding structures shown at right (see Figure 7 for G1 structure). The globally optimized GM structure is shown in top and side views at far right. Atom color codes: green: B, orange: Mg.

96 lower energy than the hexagonal arrangement exist, with six such patterns identified from  
 97 our initial search. We further note that  $\overline{CN}_{\text{B-B}(\text{surface})}$  for these lower-energy patterns tend  
 98 to be higher (up to a maximum of 4, compared with 3 for the unreconstructed hexagonal  
 99 surface), indicating a degree of  $B_{\text{surface}}$  clustering.

100 Top-view structures of the two iso-energetic surfaces with the lowest energy from our ini-  
 101 tial search (LM2, LM3) are shown alongside the pristine surface (LM1) in Figure 1. Changes  
 102 from LM1 to LM2 correspond to migrations of two adjacent  $B_{\text{surface}}$  from hollow to atop sites  
 103 along their connective path, forming symmetric 10-membered B rings and exposing two sub-  
 104 surface Mg atoms. LM3 is structurally close to LM2, containing irregular 11-membered-B  
 105 rings. Because formation of these structures results in broken B-B bonds within the hexag-  
 106 onal sheet, we denote it as a ring-opening process.

107 To explore a broader range of configurational space, we next turned to a larger 4x4 surface  
 108 model. Here, a full enumeration of  $B_{\text{surface}}$  locations becomes impractical. Instead, we created  
 109 initial structures based on optimized structures extracted from the 2x2 surface models, then  
 110 employed a Basin-Hopping global optimization scheme to access new configurations. Details  
 111 of the structure-generating procedures and all optimized structures can be found in the SI  
 112 Section 2. Relative energies of all 4x4 computed slab structures are reported in Figure 1, plot-  
 113 ted against  $\overline{CN}_{\text{B-B}(\text{surface})}$  as orange filled circles. Due to the broader configurational space,  
 114 surface patterns captured by the 4x4 surface model are generally lower in energy than the  
 115 2x2 ones at similar  $\overline{CN}_{\text{B-B}(\text{surface})}$ . This further clarifies that the conventional hexagonal ar-  
 116 rangement is merely metastable, and that it competes with a variety of possible lower-energy  
 117 arrangements. Moreover, the manifold of the lowest-energy pattern decreases monotonically  
 118 with increasing  $\overline{CN}_{\text{B-B}(\text{surface})}$ , highlighting the clustering preferences for  $B_{\text{surface}}$ , achieved  
 119 by abandoning extended hexagonal-ring structures to form larger, asymmetrical rings and  
 120 clusters. The globally optimized 4x4 surface structure, labeled as GM in the rightmost panel  
 121 of Figure 1, is 131 meV/ $B_{\text{surface}}$  lower in energy than the starting hexagonal surface. The  
 122 CIF file of GM can be found in SI. Interestingly, the surface appears to be amorphous-like

123 and highly disordered, containing a mixture of irregular 10-, 11-, 14-membered rings with  
 124 clusters of boron, such as umbrella-like  $B_7$ , and triangular  $B_6$ . This behavior is similar to  
 125 that reported for the annealed  $ZrB_2$  boron surface by Suehara *et al.* where boron atoms  
 126 cluster and form large ring structures.<sup>16</sup> Moreover, a significant fraction of subsurface Mg  
 127 atoms originally masked by  $B_{\text{surface}}$  are now exposed as a result of the  $B_{\text{surface}}$  ring opening  
 128 process. From the side view in Figure 1, it is also visually obvious that some  $B_{\text{surface}}$  atoms  
 129 in atop positions (relative to subsurface Mg) rise from the surface.

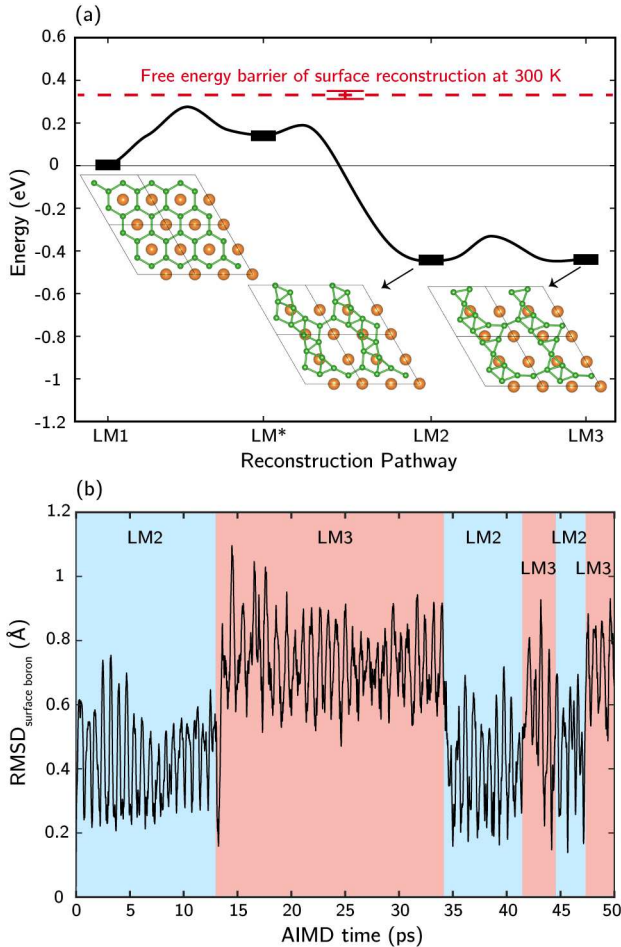


Figure 2: **Boron surface dynamics.** (a) CI-NEB-computed minimum energy paths for LM1→LM2→LM3 surface conversion (black curve), along with the metadynamics-computed free energy barrier for LM1→LM2 at 300 K (dashed red line, with error bars shown). Atom color codes: green: B, orange: Mg. (b) Root mean squared displacement (RMSD) of surface boron atoms from AIMD simulations of LM2 at 300 K, referenced to relaxed LM2 structure.

130 **Figure 2(a)** illustrates the kinetics of the surface reconfiguration process, computed

131 by tracing the reaction pathways of LM1→LM2→LM3 transformations using the climbing  
132 image nudged elastic band method (CI-NEB). As shown in Figure 2(a), the LM1→LM2 tran-  
133 sition goes through a metastable local minimum (LM\*) and has an overall zero-temperature  
134 activation energy of only 0.27 eV. The activation barrier associated with the LM2→LM3  
135 transition is even smaller,  $\sim 0.12$  eV. (The full minimum energy paths (MEPs) can be found  
136 in the SI Section 3). We also quantified the free energy of activation needed for the system  
137 to escape the LM1 state at a finite temperature using metadynamics simulations. These  
138 simulations reveal a free energy barrier of 0.33 ( $\pm 0.02$ ) eV at 300 K for conversion to LM2  
139 - slightly higher than the corresponding 0-K barrier—confirming that LM2 is the nearest  
140 local minimum to LM1 upon surface reconstruction (further details can be found in the SI  
141 Section 4). Accordingly, the kinetics of surface disordering are readily accessible even at  
142 room temperature. The low barrier in Figure 2(a) implies the likelihood that the system can  
143 interchange easily between LM2 and LM3. To confirm this, we performed AIMD simulations  
144 at 300 K. Figure 2(b) shows the dynamics of a reconstructed boron surface by monitoring  
145 the root mean squared displacement (RMSD) of surface boron atoms. Multiple episodes of  
146 LM2↔LM3 interconversion are detectable even within these short simulation timescales at  
147 room temperature, manifesting the highly dynamic nature of the boron surface. Collectively,  
148 the results point to a MgB<sub>2</sub> surface structure that disorders spontaneously and dynamically  
149 under operating conditions, in sharp contrast to the assumption of a static hexagonal ar-  
150 rangement.

151 The surprising dynamical disordering tendency of the boron surface in MgB<sub>2</sub> can be  
152 understood by analyzing the surface electronic properties in detail, as shown in **Figure 3**.  
153 Bader charge analysis was used to gain insights into the electronic origin of favorable boron  
154 surface reconstruction. For reference, we first determined the excess partial charges ( $q$ ) of  
155 Mg and B in pristine bulk MgB<sub>2</sub> from Bader analysis. The average  $q$  of Mg and B are +1.66  
156 and -0.83, respectively, corresponding qualitatively to the expected formal oxidation states  
157 of +2 and -1.

158 Next, these bulk values were compared to the average  $q$  in surface and subsurface layers  
 159 of the lowest-energy 4x4 reconstructions of the boron-terminated  $\text{MgB}_2$  surfaces. Corre-  
 160 sponding values for the unreconstructed  $\text{MgB}_2$  surface were also included in our analysis.  
 161 Figure 3(a) shows the average  $q$  of the outermost surface boron atoms ( $B_{\text{surface}}$ ) within each  
 162 computed 4x4 slab, plotted against  $\overline{CN}_{\text{B-B}(\text{surface})}$ . The average  $q$  spans a range of  $> 0.1 e$   
 163 across structures, with a minimum of about half of the  $q$  in bulk  $\text{MgB}_2$  for the hexagonal  
 164 unreconstructed surface ( $\overline{CN}_{\text{B-B}(\text{surface})} = 3$ ). Thus, missing a layer of coordination with Mg  
 165 clearly leads to partial charge depletion of  $B_{\text{surface}}$ . In addition, the average  $q$  of  $B_{\text{surface}}$   
 166 increases with  $\overline{CN}_{\text{B-B}(\text{surface})}$ , reflecting further charge depletion of  $B_{\text{surface}}$  upon additional  
 167 surface reconstruction and boron aggregation.

168 Figures 3(b) and (c) break down the average  $q$  of subsurface B and Mg by layer within  
 169 the slab models (plotted against the average  $q$  of  $B_{\text{surface}}$ ), demonstrating the heterogeneous  
 170 distribution of charge among layers. Bulk-like  $q$  is attained by the second sublayer of Mg  
 171 atoms and the third sublayer of B atoms (see figure caption for details). Strongly negative  
 172 correlations in  $q$  were found between  $B_{\text{surface}}$  atoms and their closest B and Mg sublayers,  
 173 suggesting the variation in the average  $q$  of  $B_{\text{surface}}$  across different surface configurations is  
 174 mainly due to the surface-dependent charge distribution among these three layers.

175 Overall, our charge analyses suggest that partial charge depletion of  $B_{\text{surface}}$  due to sub-  
 176 stoichiometric coordination with Mg is highly correlated with B–B bond reorganization and  
 177 energetically favorable surface disordering. It is reasonable to extrapolate this concept to  
 178 other oxidation scenarios and different surface terminations that may lead to similar behav-  
 179 ior. To test this hypothesis, we created another model system to examine direct oxygen  
 180 attack of a Mg-terminated (0001)  $\text{MgB}_2$  surface, which mimics the oxygen susceptibility  
 181 under actual operating conditions. Starting again with a 4x4 (0001) slab with four  $\text{MgB}_2$   
 182 layers, we relaxed the structure under the addition of an oxygen monolayer on the Mg sur-  
 183 face. Subsurface B have an average  $q$  of 0.38, confirming strong oxidation by surface oxygen.  
 184 Global optimization via Basin Hopping caused subsurface B atoms to undergo exothermic

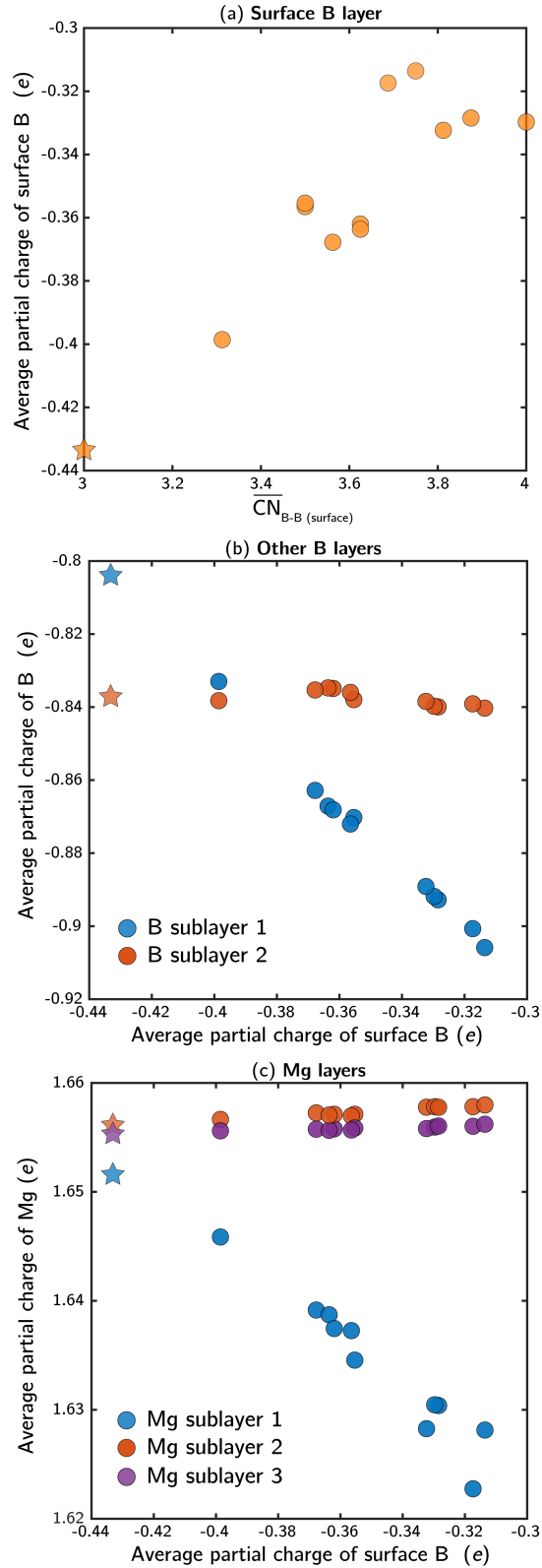


Figure 3: **Partial charge analysis.** (a) Average partial charge of surface B atoms as a function of surface B-B coordination number. Average partial charge of (b) other B layers and (c) Mg layers as a function of the average partial charge of surface B atoms. B and Mg layer indices are defined according to their proximity relative to the outermost boron surface. Data is compiled from all computed  $1 \times 1$  surface configurations in Figure 1. Stars represent the pristine hexagonal surface.

185 disordering into irregular rings and clusters very similar to the B-terminated clean surface,  
186 thus validating our hypothesis (see SI Section 5 for surface structures of locally optimized  
187 and globally optimized configurations with oxygen). We also repeated the optimization pro-  
188 cess for a slab with the Mg surface covered by atomic H (surface hydrides with 1:1 Mg/H  
189 ratio), where subsurface B have an average  $q$  of -0.81 similar to bulk B, and no subsurface B  
190 reconstruction was observed. We therefore expect that only strong oxidizing agents capable  
191 of substantially depleting the charge of the subsurface B layer would facilitate spontaneous  
192 boron layer disordering.

193 It is worth pointing out that charge depletion of the B layer at the  $\text{MgB}_2$  surface causes  
194 these atoms to approach their elemental (neutral) charge state. This provides a clue for  
195 explaining the disordering tendency. Specifically, Ogitsu *et al.* reported through a global-  
196 phase space search that elemental  $\beta$ -rhombohedral boron contains a macroscopic amount of  
197 intrinsic defects, leading to a degenerate and disordered ground state.<sup>27,28</sup> The authors were  
198 able to trace this behavior to geometrical frustration of partially occupied site configurations,  
199 which mimic frustrated spin-lattice configurations and are intrinsic to elemental boron. Sim-  
200 ilarly, Liu *et al.* found that a free-standing charge-neutral boron sheet in vacuum strongly  
201 prefers disordering and forms amorphous-like patterns. In the case of  $\text{MgB}_2$ , we propose that  
202 formation of elemental-like surface B due to substoichiometric coordination with Mg drives  
203  $\text{B}_{\text{surface}}$  into an electronic state close to elementary frustrated B substance, which introduces  
204 a degree of electronic frustration that manifests as spontaneous dynamical disordering.

## 205 **2.2 Experimental analysis of $\text{MgB}_2$ surface disordering**

206 To validate the predicted disordering of surface boron atoms, we synthesized  $\text{MgB}_2$   
207 nanosheets (NSs) with predominant boron surface termination through mechanical exfo-  
208 liation using high-energy ball milling, followed by dispersion in acetonitrile and subsequent  
209 centrifugation (see Methods)<sup>29</sup> Using transmission electron microscopy (TEM) and atomic  
210 force microscopy (AFM), we determined that the exfoliated  $\text{MgB}_2$  NSs were flat with lateral

211 dimensions ranging from 100 nm to 500 nm and thicknesses of  $\sim 4$  nm (**Figure 4(a)** and SI  
212 Section 6). The dominant  $\text{MgB}_2$  composition was confirmed using energy-dispersive X-ray  
213 spectroscopy (EDS) analysis (SI Section 6). To comment on the crystalline nature and the  
214 degree of exfoliation of  $\text{MgB}_2$ , we acquired X-ray diffraction (XRD) data of bulk and exfoli-  
215 ated  $\text{MgB}_2$  NSs (Figure 4(b)). The exfoliated  $\text{MgB}_2$  NSs show significant peak broadening,  
216 likely due to finite size/Scherrer and/or strain effects resulting from a high degree of exfoli-  
217 ation of  $\text{MgB}_2$ . Moreover, the intensity of the (001) and (002) peaks corresponding to the  
218 C-stacking planes of  $\text{MgB}_2$  is highly diminished, indicating the presence of only a few layers  
219 within the crystals.<sup>30</sup>

220 In order to confirm that the  $\text{MgB}_2$  sheets are predominantly B-terminated, we performed  
221 low energy ion scattering (LEIS), which can provide an elemental analysis of the outermost  
222 surface monolayer.<sup>31</sup> LEIS measurements of  $\text{MgB}_2$  NSs pressed into an indium foil suggest  
223 a primarily boron-terminated surface, based on two main observations. First, the presence  
224 of boron at the surface was confirmed with an ion energy spectrum taken with a 3 keV  $\text{Ne}^+$   
225 beam in Figure 4(c). This spectrum contains a large B(R) peak, corresponding to detection  
226 of surface boron being recoiled by incident  $\text{Ne}^+$  into the detector. Second, to interrogate  
227 the boron surface coverage, LEIS measurements were taken with a 3 keV  $\text{He}^+$  beam. These  
228 spectra, plotted in Figure 4(d), reveal a strong matrixing effect (neutralization of the incident  
229 ions). All higher energy peaks associated with scattering from all surface species (B, O, Mg,  
230 and In) are greatly suppressed. For comparison, the blue dotted line shows a spectrum for  
231 a clean Mg surface, which contains a large Mg(QS) peak. Similar matrixing effects have  
232 been reported for complete graphitic carbon monolayers on metal surfaces by Mikhailov et  
233 al.,<sup>32</sup> who noted that these effects may be expected to occur for other light elements strongly  
234 bonded to metals. The combination of these two observations demonstrates that boron is  
235 present at the surface and likely constitutes a large portion of the surface termination.

236 The native disordering of the boron planes near the surface was probed using X-ray  
237 absorption spectroscopy (XAS) measurements, which was previously established as a reliable

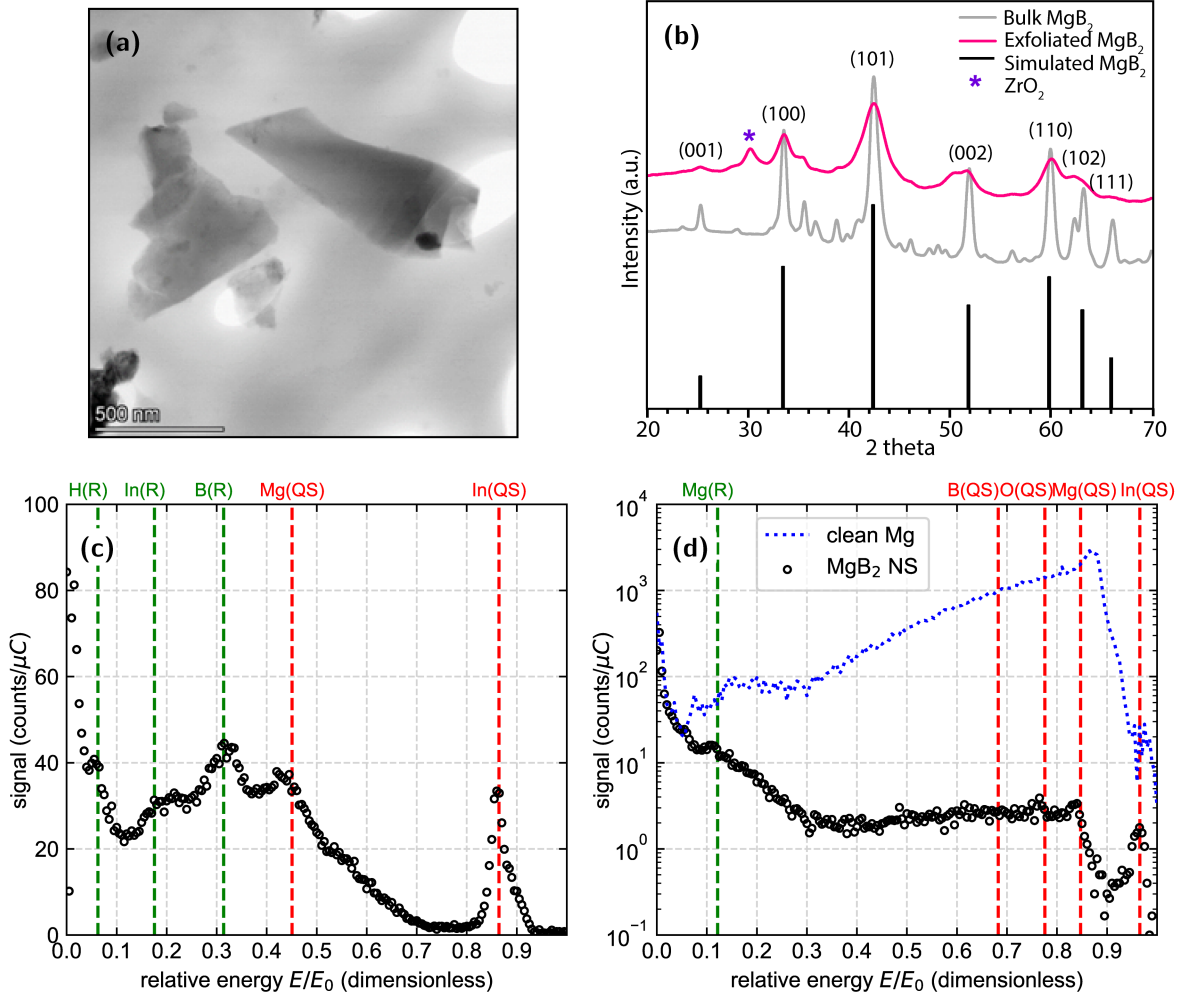


Figure 4: **Physical and chemical characterization of the exfoliated  $\text{MgB}_2$  NSs.** (a) Representative TEM image of the exfoliated  $\text{MgB}_2$  NSs, (b) XRD analysis of bulk or standard  $\text{MgB}_2$  and exfoliated  $\text{MgB}_2$  NSs are compared with simulated  $\text{MgB}_2$  diffraction data. A small peak at  $30.4^\circ$  corresponds to the zirconia ( $\text{ZrO}_2$ ) contamination obtained during high energy ball milling (HEBM) of  $\text{MgB}_2$ . (c) Ion energy spectrum for 3 keV  $\text{Ne}^+$  on the  $\text{MgB}_2$  NSs for  $\alpha = 76^\circ$  and  $\theta = 54^\circ$ . Scattering peaks are labeled X(QS) in red, while recoil peaks are labeled X(R) in green, to denote scattering or recoiling a surface atom of species X. The ion energy spectrum reveals a sizeable B(R) peak, evidence that boron is at the  $\text{MgB}_2$  NS surface. (d) Ion energy spectrum for 3 keV  $\text{He}^+$  on  $\text{MgB}_2$  NSs is plotted as open black circles for  $\alpha = 76^\circ$  and  $\theta = 60^\circ$ . For an illustrative comparison, a second ion energy spectrum for 2 keV  $\text{He}^+$  on a clean Mg surface (for  $\theta = 55^\circ$ ) is shown as a blue dotted line. The higher energy scattering peaks for the  $\text{MgB}_2$  NSs are greatly suppressed by a matrixing effect. Note that a small shift in the relative energy of the Mg(QS) peaks between the two spectra is expected, due to the slightly different scattering angle  $\theta$ .

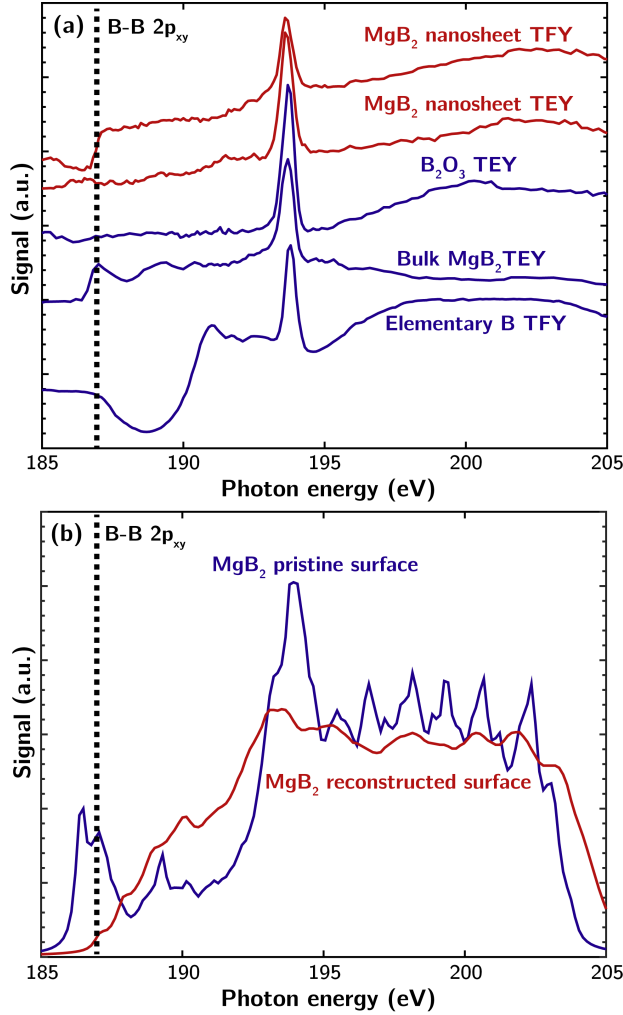


Figure 5: **XAS measurements and simulations of exfoliated MgB<sub>2</sub> NSs.** (a) Boron K-edge TEY (Total Electron Yield; surface-sensitive) and TFY (Total Fluorescence Yield; more bulk-sensitive) modes of XAS spectra for exfoliated MgB<sub>2</sub> nanosheets, compared to reference spectra for other bulk boron-containing compounds. (b) Simulated XAS spectra for MgB<sub>2</sub> slabs with pristine or GM-reconstructed boron surfaces. The decrease in the simulated signal near 203 eV is due to the finite number of electronic bands included in the calculations

238 technique for assessing the intactness of the boron ring structure.<sup>24</sup> In particular, a peak  
239 near  $\sim 187$  eV corresponds to B  $2p_{xy}$  states that are characteristic of the B-B hexagonal ring  
240 structure of bulk  $\text{MgB}_2$ .<sup>33</sup> XAS measurements of the exfoliated  $\text{MgB}_2$  NSs were performed  
241 in both TEY (total electron yield, a surface-sensitive mode) and TFY (total fluorescence  
242 yield, a more bulk-sensitive mode) modes. As shown in **Figure 5(a)**, the B-B ring feature  
243 is indeed completely missing in the TEY mode in the  $\text{MgB}_2$  NSs. The feature at 193.7  
244 eV corresponds to  $\text{B}_2\text{O}_3$  (or other sub-stoichiometric boron oxides), which indicates that  
245 some limited oxidation is occurring even in these pristine samples. However, the exfoliated  
246  $\text{MgB}_2$  NSs also show small peak-like features between 191.5 eV and 193 eV, which are not  
247 present in the  $\text{B}_2\text{O}_3$ , and similar features are observed in this range for a powder sample of  
248 elemental boron. This is consistent with our theoretical calculations suggesting that B-rich  
249 surfaces should feature complex structures with higher B coordination that are closer to  
250 neutral oxidation state, similar to those in elemental boron.

251 As further confirmation of our interpretation, we also directly simulated the B K-edge  
252 XAS spectra for pristine and reconstructed  $\text{MgB}_2$  surface layers (based on the GM recon-  
253 struction). The results are shown in Figure 5(b). Whereas the  $2p_{xy}$  feature near 187 eV  
254 is retained for the pristine surface, indicating intact surface boron rings, the reconstructed  
255 surface is indeed missing this feature. The reconstructed surface also exhibits increased  
256 spectral weight between 188 and 193 eV, including a small peak near 190 eV and shoulder  
257 near 191.5 eV that are reminiscent of similar features between 191.5 eV and 192.5 eV in the  
258 exfoliated  $\text{MgB}_2$  B K-edge TEY XAS measurements (Figure 5(a)). Thus, the XAS signature  
259 of the theoretically predicted surface reconstruction is consistent with spectrum of the ex-  
260 foliated  $\text{MgB}_2$  B K-edge TEY XAS measurements, strongly supporting the hypothesis that  
261 the disruption of the hexagonal ring structure produces substantial surface disorder.

## 2.3 Implications for $\text{MgB}_2$ surface reactivity

The native surface disorder introduces heterogeneity in local surface properties of  $\text{MgB}_2$ , with potentially broad implications for application performance. As one illustration, **Figure 6** explores the interaction of disordered  $\text{MgB}_2$  with hydrogen in view of its utility as a hydrogen storage material.<sup>3</sup> Liu *et al.* proposed that the intrinsic stability of the B–B extended hexagonal ring structure hinders the overall hydrogenation kinetics of  $\text{MgB}_2$  (with an underlying assumption that B maintains hexagonal patterns even when surface-exposed).<sup>33</sup> As such, it is critical to understand which factors can facilitate B–B bond disruption. The current study suggests that such disruption is achievable natively at surfaces due to surface disordering, prompting a more direct investigation into the implications for hydrogenation.

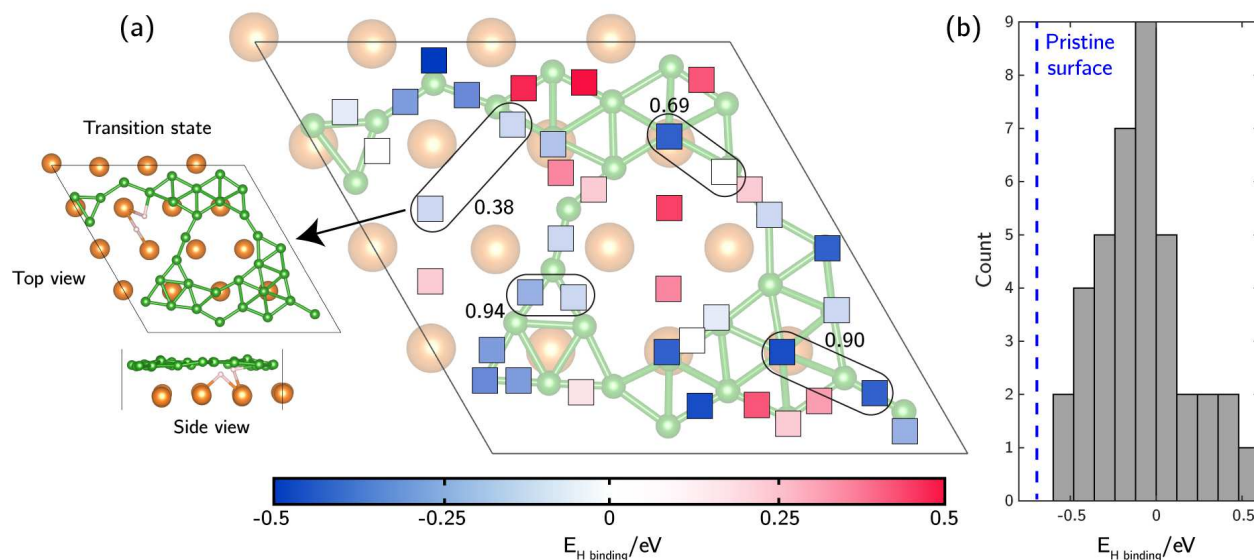


**Figure 6: Implications for  $\text{MgB}_2$  hydrogenation.** (a) Energy map of atomic H binding on the GM configuration of  $\text{MgB}_2$ , with squares indicating locally stable binding sites colored according to  $E_{\text{H binding}}$ . Tested site pairs for dissociative  $\text{H}_2$  adsorption are highlighted as black ovals, with corresponding dissociation barriers indicated in eV. Top and side views of the transition state structure for dissociative  $\text{H}_2$  adsorption at the Mg+B site pair are shown at left. Atom color codes: green: B, orange: Mg, pink: H. (b) Histogram of  $E_{\text{H binding}}$  on the GM configuration compared with the reference value for the hexagonal boron surface (vertical dashed line).

For reference, we first computed single atomic H binding to a bridge site on the unre-

273 constructed hexagonal  $\text{MgB}_2$  surface, finding a H binding energy of  $E_{\text{H binding}} = -0.68$  eV  
274 (referenced to  $\text{H}_2$  gas). To perform a similar analysis on the disordered  $\text{MgB}_2$  surface, we  
275 enumerated all possible bridge boron sites and accessible subsurface hollow Mg sites on the  
276 GM configuration. Figure 6(a) reports all local minima identified after geometry optimiza-  
277 tions, colored by the computed  $E_{\text{H binding}}$ . A strong site-dependent heterogeneity is observed,  
278 spanning a range from -0.5 to 0.5 eV, as highlighted in the histogram in Figure 6(b). Over-  
279 all, interactions between the boron surface and H are weakened after surface disordering.  
280 Perhaps more importantly, the large range of energies indicates an especially large variety  
281 of intrinsic local reactivities.

282 The  $\text{H}_2$  dissociation kinetics exhibit a similarly wide range of local intrinsic variability  
283 on disordered  $\text{MgB}_2$ . From zero-temperature CI-NEB, the reference surface  $\text{H}_2$  dissociation  
284 barrier onto two neighboring bridge sites of the unreconstructed hexagonal  $\text{MgB}_2$  surface  
285 is found to be 0.52 eV (full MEP can be found in SI Section 7). Figure 6(a) reports the  
286 calculated  $\text{H}_2$  dissociation kinetics on three representative pairs of neighboring H binding  
287 sites on the disordered GM  $\text{MgB}_2$  surface with different relative pairings of  $E_{\text{H binding}}$  values.  
288 We also included in our analysis a site pair consisting of a subsurface Mg site and a site  
289 on surface B (detailed MEPs can be found in SI Section 7). Dissociation barriers at the  
290 three paired-B sites are all higher than on the pristine hexagonal surface, suggestive of lower  
291 reactivity of the  $\text{B}_{\text{surface}}$  alone with  $\text{H}_2$  upon surface disordering. However, dissociation on  
292 the surface B and subsurface Mg sites is more facile (0.38 eV). The transition state structure,  
293 reported in Figure 6(a), shows that as  $\text{H}_2$  begins to dissociate, it stays in close contact with  
294 both  $\text{B}_{\text{surface}}$  and subsurface Mg. The Lewis acid-base pair interaction created by the Mg  
295 and B (see Figure 3(a) and (c)) polarizes the  $\text{H}_2$  molecule, stabilizing the transition state  
296 structure and facilitating H–H bond cleavage. Indeed, our calculations confirm that at the  
297 transition state, the two H atoms have opposite partial charges of -0.5 and +0.05 for the  
298 Mg-bonded and B-bonded H, respectively.

299 As a result, exposure of subsurface Mg upon boron surface disordering introduces a new

300 mechanism for facile  $\text{H}_2$  dissociation on select sites. Under hydrogenation conditions, it is  
301 reasonable to assume that such sites could function as the predominant “scissors” for  $\text{H}_2$   
302 cleavage. As exothermic atomic H diffusion is expected to be facile, exemplified by low  
303 H diffusion barriers<sup>34</sup> in bulk  $\text{MgB}_2$ , and on the pristine Mg-terminated (0001) surfaces,<sup>35</sup>  
304 the resulting atomic H can then diffuse to other nearby favorable binding sites. However,  
305 one caveat is the lower density of sites with negative  $E_{\text{H binding}}$ , which may prevent the  
306 disordered surface from attaining a high H coverage (assuming all  $B_{\text{surface}}$  remain intact  
307 during hydrogenation). Accordingly, the disordered surface is likely to exhibit a competition  
308 between site activity and coverage (site density).

## 309 2.4 Surface disordering of other diborides

310 Inspired by our findings for  $\text{MgB}_2$ , we performed a general assessment of surface disordering  
311 tendency for a diverse set of metal diborides with the  $P6/mmm$  space group that have been  
312 researched and reported in the literature, with metals ranging from s-metals (Mg, Al), first-  
313 row transition d-metals (Sc, Ti, V, Mn), late transition d-metals (Nb, Ta, Mo, Zr, Hf) and  
314 f-elements (U). For each metal diboride, we simulated the modest surface distortion found for  
315  $\text{MgB}_2$  shown in **Figure 7(a)** that is labeled as G1 in Figure 1. Relaxed structures remained  
316 similar to their initial configurations for most diborides, except for  $\text{FeB}_2$  and  $\text{YB}_2$ , which  
317 underwent significant spontaneous structural reorganization following initial distortion, as  
318 illustrated in SI Section 8. Figure 7(b) reports the reaction energies ( $\Delta E$ ) associated with  
319  $B_{\text{surface}}$  disordering for each metal diboride.  $\Delta E$  varies significantly across different diborides,  
320 spanning both positive and negative regimes.

321 Overall, we predict that  $\text{ScB}_2$ ,  $\text{MnB}_2$ ,  $\text{MgB}_2$ ,  $\text{YB}_2$ , and  $\text{FeB}_2$  should all exhibit native  
322 surface disordering, with  $\text{FeB}_2$  showing the strongest reconstruction tendency. In these sub-  
323 stances, the average partial charges of surface boron atoms, particularly in  $\text{MnB}_2$  and  $\text{FeB}_2$   
324 (-0.22 and -0.15, respectively), are all less negative than that in  $\text{MgB}_2$  (-0.42). Beyond  
325 the energetic benefits, surface disordering also enhances configurational entropy, which may

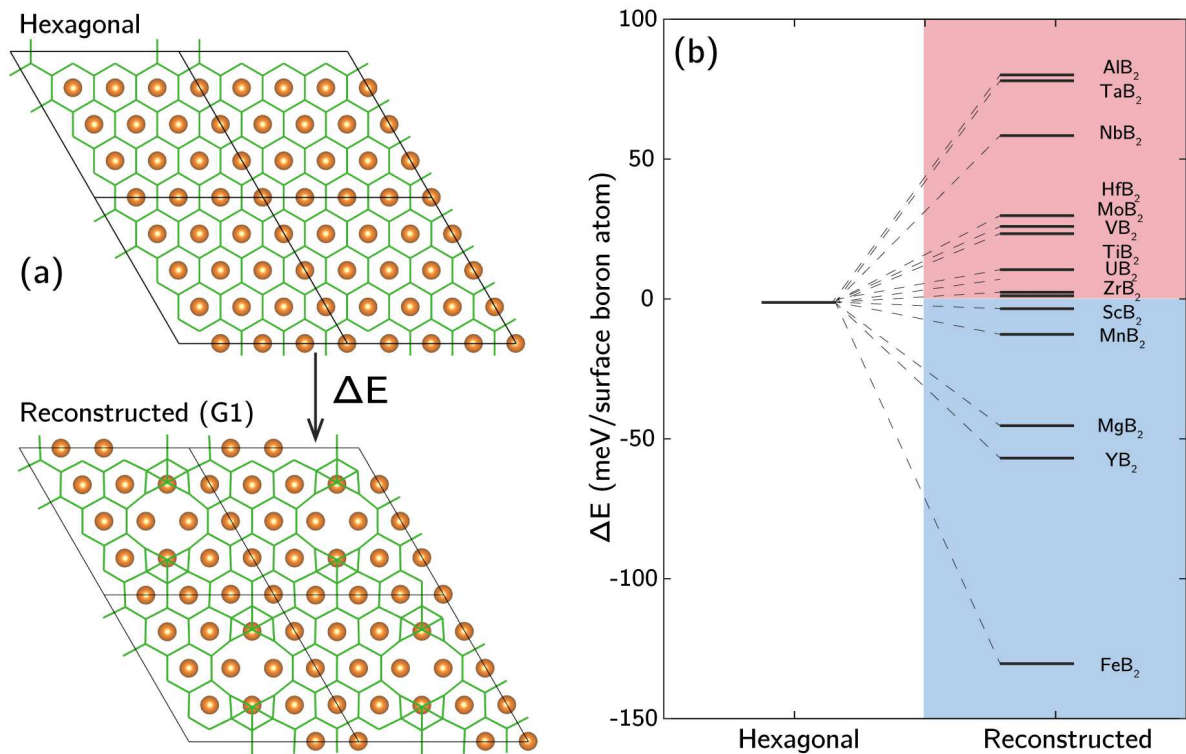


Figure 7: **Predictions of surface disordering for other metal diborides.** (a) Structures of the pristine hexagonal and modestly distorted  $\text{MB}_2$  boron surfaces used as initial configurations to assess surface disordering tendency. Atom color codes: green: B, orange: M. (b) Energy diagram of final boron surface configurations following structural relaxation from G1, referenced to the hexagonal boron surface. Colors distinguish metal diborides exhibiting endothermic reconstruction (pink) from those exhibiting exothermic reconstruction (blue).

326 lead to additional stabilization for diborides that are slightly positive in  $\Delta E$ . This provides  
327 a rationalization for observations of reconstructed  $\text{ZrB}_2$  by Suehara *et al.*<sup>16</sup> Moreover, the  
328 linkage between metal oxidation tendency and surface disordering tendency suggests that  
329 disordering could be induced in other diborides by substitutional doping of elements such as  
330 Mg, Y, or Fe, or suppressed by doping with Al, Ta, or Nb, etc. Note that the analysis in Fig-  
331 ure 7 only covers  $\text{MB}_2$  systems with a stoichiometric M-to-B ratio of 1:2. However, addition  
332 or depletion of boron vacancies resulting in other surface boron densities and patterns are  
333 also possible, as has been widely reported for borophenes and other quasi-2D nanostructures  
334 obtained from metal borides like  $\text{AlB}_2$  and  $\text{TiB}_2$ .<sup>36,37</sup>

### 335 **3 Discussion**

336 In conclusion, our results unravel a previously unrecognized spontaneous surface disordering  
337 phenomenon of boron surfaces of  $\text{MgB}_2$  and certain related metal diborides. This disordering  
338 can be linked to the formation of frustrated surfaces that mimic the known complex behavior  
339 of elemental boron. The behavior was confirmed in synthesized  $\text{MgB}_2$  nanosheets, which  
340 showed spectral evidence that is consistent with native disordering of the boron hexagonal  
341 ring structure. Moreover, this surface atomic reorganization is predicted to be dynamic,  
342 suggesting local surface bonding character in fact fluctuates.

343 One immediate consequence of our findings is that idealized surface models may give  
344 a misleading picture of the surface-relevant properties of metal diborides. Computational  
345 models generally assume hexagonal B surfaces for such compounds;<sup>22,25,38</sup> while such an as-  
346 sumption may hold true for some metal diborides, mechanistic interpretations for others can  
347 be inaccurate. Moreover, when accurate surface energies are required, as in the prediction of  
348 properties of nanosized metal diborides, hexagonal surface models that do not account for  
349 stabilization upon disordering may not be sufficiently representative. Likewise, when screen-  
350 ing surface activity based on relevant computed descriptors, for instance using H binding

351 energy to an active site to infer its hydrogen evolution reaction activity,[29] an accurate  
352 determination of surface arrangement is a prerequisite.

353 In addition, our work points to important practical consequences. Because disordered  
354 surfaces exhibit a broader heterogeneity of local properties, this new understanding of the  
355 nature of the boron surface also has nonobvious implications for performance. One example  
356 lies in the increased richness of hydrogenation chemistry for hydrogen storage applications,  
357 for which surface disordering of  $\text{MgB}_2$  was found to expose a new  $\text{H}_2$  dissociation pathway  
358 that leverages Lewis acid-base pair interactions to significantly lower barriers. At the same  
359 time, it provides insight into how the stability of boron ring structures may be altered,  
360 which has been suggested as a first step towards rupturing the  $\text{MgB}_2$  lattice and promoting  
361 phase transformations during later-stage hydrogenation. This highlights the necessity of  
362 considering the surface atomic disordering in interrogation of mechanisms and interpretation  
363 of experimental observations, while simultaneously guiding approaches for improvement.

364 Finally, we point out that the rich structural diversity of patterned borophenes has al-  
365 ready generated intense interest due to the variety of potentially tunable properties. We  
366 suggest that natively disordered boron surfaces can extend this catalog to include amor-  
367 phous variants. Indeed, our study points to a possible engineering strategy for generating  
368 surface disorder in diborides via substitutional doping of metals with higher primary ox-  
369 idation states, which opens up a new avenue for exploration of amorphous borophenes with  
370 a wider variety of compositions. This is particularly notable in light of recent interest in  
371 high-entropy alloys of metal diborides,<sup>39</sup> which offer a diverse palette for altering compo-  
372 sition. The potential tunability prompts the possibility of engineering boron surfaces of  
373 nanoscale and 2D systems with specifically tailored properties—for instance, for use in coat-  
374 ings, composites, electronic materials, or device applications.<sup>40,41</sup> Likewise, the diversity of  
375 binding configurations due to the presence of surface disorder could be an important tool for  
376 realizing multifunctional catalytic applications.<sup>30,42</sup>

## 4 Methods

### 4.1 Computational Methods

#### 4.1.1 DFT Calculations

Plane-wave, periodic supercell DFT calculations were performed with the Vienna ab initio simulation package (VASP), version 5.4.4,<sup>43</sup> using the projector augmented wave treatment of core-valence interactions<sup>44,45</sup> with the Perdew-Burke-Ernzerhof (PBE)<sup>46</sup> generalized gradient approximation for the exchange-correlation energy. Initial bulk structures of metal diborides were obtained from the Materials Project.<sup>47</sup> Enumeration of symmetry-distinct initial configurations was performed using the enumlib code<sup>48</sup> wrapped in pymatgen.<sup>49</sup> Supercell generations were facilitated by the Atomic Simulation Environment (ASE) package.<sup>50</sup> To model (0001) boron surface, we first cleaved the bulk MgB<sub>2</sub> into a (0001) 2x2 stoichiometric slab with four MgB<sub>2</sub> layers, each with 8 boron and 4 Mg atoms. Each slab is separated from periodic images by at least 15 Å of vacuum. Such slab separation by vacuum was confirmed to be sufficient by Effective Screening Medium<sup>51</sup> calculations implemented in Quantum Espresso<sup>52</sup> that showed negligible dipole-dipole interactions of slabs cross periodic images along z-direction. The bottom two layers containing Mg surface were fixed, and the top two layers including the boron surface are allowed to fully relax. To further sample the configurational space of boron surface atomic arrangements, we quadrupled the surface size to 4x4 to reduce translational symmetry imposed by periodic boundary conditions, maintained the slab thickness and performed a selection of geometry optimizations and Basin-Hopping global optimizations. For all calculations, the energy cutoff for the plane-wave basis set was set to 500 eV, self-consistent-field electronic energies were converged to 10<sup>-4</sup> eV and atomic forces to less than 0.03 eV/Å. Spin-polarization was turned off in general, unless specified, as most materials simulated are nonmagnetic. The Brillouin zone was sampled with a  $\Gamma$ -centered 4x4x1 k-point mesh for 2x2 slab structures, and a  $\Gamma$ -centered 3x3x1 k-point mesh

402 for 4x4 slab structures. We deem such k-point sufficient as test calculations for MgB<sub>2</sub> with  
 403 higher k-point density cause only negligible differences in relative energies across structures  
 404 with the same lattice. K-points were reduced to 2x2x1 for climbing-image nudged elastic  
 405 band (CI-NEB)<sup>53,54</sup> calculations for 4x4 slabs, but maintained as 4x4x1 for 2x2 slabs, allow-  
 406 ing direct energetics comparisons. Bader charge analyses were performed using the algorithm  
 407 developed by Henkelman *et al.*<sup>55-57</sup> For atomic H binding calculations, binding strength were  
 408 quantified by referencing to gas phase H<sub>2</sub> following

$$E_{\text{H binding}} = E_{\text{surface+H}} - E_{\text{surface}} - \frac{1}{2}E_{\text{H}_2} \quad (1)$$

409 where  $E_{\text{surface+H}}$ ,  $E_{\text{surface}}$  and  $E_{\text{H}_2}$  are DFT-computed energies of a surface with an adsorbed  
 410 atomic H, the adsorbate-free clean surface and H<sub>2</sub> in gas phase, respectively.

#### 411 4.1.2 *Ab initio* Molecular Dynamics and Metadynamics Simulations

412 NVT *ab initio* molecular dynamics (AIMD) were performed for 2x2 slabs with the energy  
 413 cutoff for the plane-wave basis set reduced to 400 eV and the Brillouin zone sampled with a  
 414  $\Gamma$ -centered 3x3x1 k-point mesh. Timestep was set to 1 fs and a Nose-Hoover thermostat was  
 415 used to maintain the temperature. To quantify the dynamics of boron surfaces, root mean  
 416 square displacement (RMSD) of surface boron atoms in the course of AIMD trajectories were  
 417 collected after 3 ps of pre-equilibrating for each system. To compute the free energy bar-  
 418 rier of surface reconstruction at finite temperatures, metadynamics was performed starting  
 419 with the 2x2 pristine slab. Metadynamics is a nonequilibrium molecular dynamics method  
 420 capable of efficiently sampling free energy surfaces of complex reactions.<sup>58</sup> As surface recon-  
 421 struction requires B–B bond breaking of the pristine surface, we selected the coordination  
 422 number of an arbitrary pair of bonded surface boron atoms as the collective variable (CV),  
 423 mathematically defined as

$$\frac{1 - \left(\frac{d_{ij}}{d_0}\right)^9}{1 - \left(\frac{d_{ij}}{d_0}\right)^{14}} \quad (2)$$

424 where  $d_{ij}$  is the actual distance between B  $i$  and  $j$ , and  $d_o$  is the reference distance as the  
425 boundary of being bonded or not between the two atoms which was set to 2 Å.

426 3 ps of AIMD was run to pre-equilibrate the system before bias potentials were introduced.  
427 Gaussian potentials, with a height of 0.002 eV and a width of 0.02, were then added to the  
428 defined CV every 10 fs. Following a previously reported protocol,<sup>59</sup> we terminated a run  
429 of metadynamics simulation after the first barrier crossing from the reactant basin into the  
430 target product basin, and computed the free energy barrier by summing up the amount of  
431 bias potentials accumulated in the reactant basin. Error bars were computed on the basis  
432 of three replicas starting with different initial configurations.

### 433 4.1.3 Basin-Hopping Global Optimization

434 Global optimizations based on the Basin-Hopping algorithm,<sup>60,61</sup> implemented in ASE, were  
435 performed for several 4x4 slab structures for which exhaustive configurational sampling was  
436 computationally demanding. In each Basin-Hopping step, only selective atoms expected  
437 to reconstruct *a posteriori* were randomly displaced around the initial position following a  
438 Gaussian distribution with a variance of 0.15 Å. From there a local structure optimization was  
439 performed and the final energy was used to accept or reject this move in the Metropolis Monte  
440 Carlo algorithm. The temperature was set to 600K which allowed systems to temporarily  
441 visit high-energy local minima in order to reach other local minima potentially barred by  
442 huge “barriers”. As Basin-Hopping requires extensive local optimizations, atomic forces were  
443 only converged to 0.20 eV/Å for each step with energy cutoff for the plane-wave basis set  
444 reduced to 400 eV, and Brillouin zone sampled at  $\Gamma$  point only. The lowest-energy structures  
445 obtained were then re-optimized following higher-accuracy DFT parameters, energy, and  
446 force criteria described in the previous section.

#### 447 4.1.4 X-ray absorption spectra (XAS) simulations

448 XAS simulations of the B K-edge were performed using first principles density functional  
449 theory within the the Vienna ab initio simulation package (VASP), version 5.4.4.,<sup>43</sup> A plane-  
450 wave cutoff of 600 eV was used and the k-point sampling was chosen such that the density of  
451 k-points is  $\geq 64\,000$  per  $\text{\AA}^{-3}$ . The XAS/XES simulations were carried out in the VASP using  
452 an implementation that computes the required matrix elements within the PAW formalism  
453 including a self-consistent treatment of the core-hole effects on the unoccupied states.<sup>62</sup>  
454 Spectra were broadened with a 0.25 eV gaussian.

## 455 4.2 Experimental methods

### 456 4.2.1 Synthesis and Preparation of $\text{MgB}_2$ nanosheets

457  $\text{MgB}_2$  powder (Sigma-Aldrich,  $\geq 99\%$  purity, 100 mesh size) was subjected to solid-state  
458 mechanical exfoliation using a high energy ball mill (HEBM, SPEX SamplePrep, 8000M  
459 Mixer/Mill). The process was carried out in a zirconia ( $\text{ZrO}_2$ ) vial using 10 mm diameter  
460  $\text{ZrO}_2$  balls. Briefly, 0.80 g of  $\text{MgB}_2$  powder and 20.16 g of  $\text{ZrO}_2$  balls were weighed in the  
461 argon glove box ( $\leq 0.1$  ppm  $\text{O}_2$  and  $\text{H}_2\text{O}$ ) and added to the milling vial to obtain a ball to  
462 powder weight ratio of 25:1. The milling vial was closed tightly in the argon glove box and  
463 then subjected to HEBM for four hours. The milled powder was collected in a glove-box  
464 and stored in a vial.

465 To separate the exfoliated nanosheets (NSs) from the milled powder, we added 90 mL of  
466 dry acetonitrile (ACN) to 0.64 g of milled  $\text{MgB}_2$  powder. The suspension ( $\text{MgB}_2/\text{ACN}$ ) was  
467 mixed using a bath ultra sonicator (Cole-Parmer 8891 Ultrasonic cleaner) for 5 minutes. The  
468 obtained dark black uniform mixture was exposed to centrifugation (Eppendorf centrifuge-  
469 5430R) at 1500 rpm for 45 minutes to separate the heavier fraction. The top supernatant  
470 was collected and left undisturbed overnight to allow other heavier fractions to settle down.  
471 After settling, the top black and clear supernatant was collected, which remains a stable

472 uniform dispersion and exhibits a strong Tyndall effect. The obtained uniform dispersion of  
473  $\text{MgB}_2$  NSs in ACN was subjected to freeze-drying (lyophilization) to recover the nanosheets  
474 in the powder form. The dry  $\text{MgB}_2$  powder was collected in a vial and stored in a glove box  
475 until further analysis.

476 Freeze-drying (lyophilization) was performed by taking the dispersion of  $\text{MgB}_2$  NSs in  
477 ACN ( 70 mL) in two 50 mL centrifuge tubes and freezing them at  $-80\text{ }^\circ\text{C}$  overnight. The  
478 frozen samples were subsequently placed in a lyophilizer (SP Scientific, VirTis BenchTop  
479 Freeze Dryer) for up to 72 hours to obtain a powder of  $\text{MgB}_2$  NSs.

#### 480 **4.2.2 Characterizations**

481 Powder X-ray diffraction measurements were recorded on an Oxford Diffraction Supernova  
482 in capillary mode using  $\text{Cu K}\alpha$  radiation, with a CCD detector at 77 mm from the samples  
483 and an exposure time of 66 seconds. The recorded 2D diffraction images were integrated  
484 to produce a 1D diffraction spectrum. The powder samples were packed in 0.7 or 0.5 mm  
485 diameter glass capillaries sealed with silicone grease under argon.

486 Transmission electron microscopy (TEM) imaging and energy-dispersive X-ray spec-  
487 troscopy (EDS) were recorded on a Thermo Fisher Titan Themis Z TEM operated at 300  
488 kV. Samples for TEM analysis were prepared by taking a small amount of  $\text{MgB}_2$  nanosheets  
489 powder and dispersed in 10 ml of dry toluene using a bath ultrasonicator for 5 minutes. Two  
490 drops ( 20  $\mu\text{L}$ ) of the dispersion were drop casted on a 300 mesh copper TEM grid coated  
491 with a lacey carbon film. The grid was air-dried for a few minutes and stored in a vial until  
492 analysis.

493 Atomic Force Microscope (AFM) images were acquired with a Dimension ICON (Bruker)  
494 contained in an argon glovebox. The AFM was operated in Peak-Force Tapping mode with a  
495 nominal tapping force of 1 nN. The tip used was a PFQNE-AL (Bruker) with spring constant  
496 of 0.84 nN/nm. Samples for AFM analysis were prepared by static dispensing of the  $\text{MgB}_2$   
497 NSs dispersion ( $\sim 20\text{ }\mu\text{L}$ ) on a cleaned and UV Ozone treated Si/ $\text{SiO}_2$  substrate and spin-

498 coated at a speed of 3000 rpm for 30 s at 100 ramp rate. The coated substrate was kept in  
499 a box and stored under an argon environment until analysis.

500 The surface termination of the  $\text{MgB}_2$  nanosheets was investigated with low energy ion  
501 scattering (LEIS) and direct recoil spectroscopy (DRS). These measurements were performed  
502 with an angle-resolved ion energy spectrometer (ARIES), which has been described in detail  
503 in previous works.<sup>63,64</sup> LEIS and DRS are complementary techniques, performed simultane-  
504 ously, with sensitivity to the masses of atoms in the outermost monolayers of a surface. LEIS  
505 and DRS are performed by directing a low energy ion beam ( $\text{He}^+$  and  $\text{Ne}^+$  for this work)  
506 at a grazing angle  $\alpha$  onto the target surface. An electrostatic analyzer (ESA) is positioned  
507 in the forward scattering direction at a chosen scattering angle  $\theta$  to detect the energies of  
508 scattered incident ions and recoiled target ions to perform LEIS and DRS, respectively. From  
509 the energies of the detected ions and the scattering angle  $\theta$ , the mass of surface atoms can  
510 be calculated, yielding insight into the surface composition. One key consideration is that  
511 the ESA detects only scattered and recoiled ions; incident ions neutralized by the surface,  
512 as well as recoiled neutral atoms, are not detected. As such, neutralization effects can play  
513 a substantial role in the obtained ion energy spectra.

514 X-ray absorption spectra (XAS) measurements of boron K-edge were acquired at beam-  
515 lines 7.3.1 and 8.0.1.4 at the Advanced Light Source (ALS), Lawrence Berkley National  
516 Laboratory (LBNL) and the REIXS beamline of the Canadian Light Source (CLS). Data  
517 was simultaneously collected in surface-sensitive total electron yield (TEY) measured as the  
518 drainage current from the sample and bulk-sensitive fluorescence yield (FY) measured using  
519 a channeltron electron multiplier. Spectra were normalized by dividing by incident beam  
520 intensity, which is monitored by drainage current from a gold grid located in the path of  
521 the x-ray beam immediately before the measurement chamber. A linear background was  
522 subtracted, and the absorption edge step was scaled to 1, taking the difference between  
523 pre-edge ( $<180$  eV) and post-edge ( $>215$  eV). The energy shift between different beamlines  
524 was calibrated using the primary peak of a  $\text{B}_2\text{O}_3$  standard. Samples were transferred into

525 the beamlines using vacuum suitcases (ALS) or a glove bag (CLS) to minimize exposure to  
526 atmospheric oxygen and moisture. The operating pressure of the endstations is better than  
527  $1 \times 10^{-9}$  Torr.

## 528 **Supporting Information Available**

529 Details of surface model, structure generation procedures, 4x4 surface structural searching  
530 scheme, and metadynamics simulations; structures of 2x2 local minima surfaces, unoptimized  
531 and optimized surface configurations with oxygen, and reconstructed  $\text{FeB}_2$  and  $\text{YB}_2$  sur-  
532 faces; minimum energy paths of surface reconstruction and  $\text{H}_2$  dissociation (PDF); additional  
533 experimental characterization results of  $\text{MgB}_2$  NSs (PDF)

## 534 **Acknowledgement**

535 The authors acknowledge financial support through the Hydrogen Storage Materials Ad-  
536 vanced Research Consortium (HyMARC) of the U.S. Department of Energy (DOE), Office  
537 of Energy Efficiency and Renewable Energy, Fuel Cell Technologies Office under Contract  
538 DE-AC52-07NA27344. This work was performed under the auspices of the DOE by Lawrence  
539 Livermore National Laboratory (LLNL) under Contract DE-AC52-07NA27344. Sandia Na-  
540 tional Laboratories is a multimission laboratory managed and operated by National Tech-  
541 nology and Engineering Solutions of Sandia, LLC., a wholly owned subsidiary of Honeywell  
542 International, Inc., for the U.S. Department of Energy's National Nuclear Security Admin-  
543 istration under contract DE-NA-0003525. We thank Josh Whaley for his assistance with  
544 ion-scattering experiments. Computing resources were provided under the LLNL Institu-  
545 tional Computing Grand Challenge program.

546 The views and opinions of the authors expressed herein do not necessarily state or reflect  
547 those of the United States Government or any agency thereof. Neither the United States  
548 Government nor any agency thereof, nor any of their employees, makes any warranty,

549 expressed or implied, or assumes any legal liability or responsibility for the accuracy,  
550 completeness, or usefulness of any information, apparatus, product, or process disclosed, or  
551 represents that its use would not infringe privately owned rights.

552

## 553 **Author contributions**

554 S.L. conceived the project. S.L., V.S. and B.C.W. coordinated the project. K.G.R.  
555 performed the XAS simulations. S.L., P.X., S.K. performed the atomistic simulations. C-S.  
556 Wong performed the LEIS experiments, with assistance from R.D.K. H.G. performed the  
557 synthesis of MgB<sub>2</sub> materials, XRD, and EDS experiments. J.D.S. performed the TEM  
558 experiments, and R.D.F. collected the AFM images. H.G., Y-S.L., A.B., and J.L. performed  
559 the XAS experiments. S.L., H.G., C-S. Wong, K.G.R., and B.C.W. wrote the manuscript  
560 and prepared the figures with help from the other co-authors. All the authors contributed  
561 to the scientific discussions, data analysis, and preparation of the manuscript.

562

## 563 **Competing interests**

564 The authors declare no competing interests.

## 565 **References**

- 566 (1) Zhang, Z.; Penev, E. S.; Yakobson, B. I. Two-dimensional Boron: Structures, Properties  
567 and Applications. *Chem. Soc. Rev.* **2017**, *46*, 6746–6763.
- 568 (2) Li, Q.; Kolluru, V. S. C.; Rahn, M. S.; Schwenker, E.; Li, S.; Hennig, R. G.; Darancet, P.;  
569 Chan, M. K. Y.; Hersam, M. C. Synthesis of borophane polymorphs through hydro-  
570 genation of borophene. *Science* **2021**, *371*, 1143–1148.
- 571 (3) Møller, K. T.; Fogh, A. S.; Paskevicius, M.; Skibsted, J.; Jensen, T. R. Metal Boro-  
572 hydride Formation from Aluminium Boride and Metal Hydrides. *Phys. Chem. Chem.*  
573 *Phys.* **2016**, *18*, 27545–27553.

- 574 (4) Mudgel, M.; Awana, V. P. S.; Kishan, H.; Felner, I.; Alvarez, D. G. A.; Bhalla, G. L.  
575 Superconductivity of Various Borides: The Role of Stretched c-parameter. *J. Appl.*  
576 *Phys.* **2009**, *105*, 07E313.
- 577 (5) Guo, F.; Wu, Y.; Ai, X.; Chen, H.; Li, G.-D.; Chen, W.; Zou, X. A Class of Metal  
578 Diboride Electrocatalysts Synthesized by a Molten Salt-assisted Reaction for the Hy-  
579 drogen Evolution Reaction. *Chem. Commun.* **2019**, *55*, 8627–8630.
- 580 (6) Jothi, P. R.; Zhang, Y.; Yubuta, K.; Culver, D. B.; Conley, M.; Fokwa, B. P. T.  
581 Abundant Vanadium Diboride with Graphene-like Boron layers for Hydrogen Evolution.  
582 *ACS Appl. Mater. Interfaces* **2019**, *2*, 176–181.
- 583 (7) Park, H.; Zhang, Y.; Scheifers, J. P.; Jothi, P. R.; Encinas, A.; Fokwa, B. P. T.  
584 Graphene- and Phosphorene-like Boron Layers with Contrasting Activities in Highly  
585 Active Mo<sub>2</sub>B<sub>4</sub> for Hydrogen Evolution. *J. Am. Chem. Soc.* **2017**, *139*, 12915–12918,  
586 PMID: 28871784.
- 587 (8) Park, H.; Encinas, A.; Scheifers, J. P.; Zhang, Y.; Fokwa, B. P. T. Boron-Dependency  
588 of Molybdenum Boride Electrocatalysts for the Hydrogen Evolution Reaction. *Angew.*  
589 *Chem. Int. Ed.* **2017**, *56*, 5575–5578.
- 590 (9) Lee, E.; Park, H.; Joo, H.; Fokwa, B. P. T. Unexpected Correlation Between Boron  
591 Chain Condensation and Hydrogen Evolution Reaction (HER) Activity in Highly Active  
592 Vanadium Borides: Enabling Predictions. *Angew. Chem. Int. Ed.* **2020**, *59*, 11774–  
593 11778.
- 594 (10) Park, H.; Zhang, Y.; Lee, E.; Shankhari, P.; Fokwa, B. P. T. High-Current-Density  
595 HER Electrocatalysts: Graphene-like Boron Layer and Tungsten as Key Ingredients in  
596 Metal Diborides. *ChemSusChem* **2019**, *12*, 3726–3731.
- 597 (11) Gao, H.; Zhang, X.; Li, W.; Zhao, M. Tunable Broadband Hyperbolic Light Dispersion  
598 in Metal Diborides. *Opt. Express* **2019**, *27*, 36911–36922.

- 599 (12) Maity, T. N.; Gopinath, N. K.; Janardhanraj, S.; Biswas, K.; Basu, B. Computational  
600 and Microstructural Stability Analysis of Shock Wave Interaction with NbB<sub>2</sub>-B<sub>4</sub>C-  
601 Based Nanostructured Ceramics. *ACS Appl. Mater. Interfaces* **2019**, *11*, 47491–47500,  
602 PMID: 31580640.
- 603 (13) Ziemnicka-Sylwester, M. TiB<sub>2</sub>-Based Composites for Ultra-High-Temperature Devices,  
604 Fabricated by SHS, Combining Strong and Weak Exothermic Reactions. *Materials*  
605 **2013**, *6*, 1903–1919.
- 606 (14) Jordan, L. R.; Betts, A. J.; Dahm, K. L.; Dearnley, P. A.; Wright, G. A. Corrosion and  
607 Passivation Mechanism of Chromium Diboride Coatings on Stainless Steel. *Corros. Sci.*  
608 **2005**, *47*, 1085 – 1096.
- 609 (15) Mazánek, V.; Nahdi, H.; Luxa, J.; Sofer, Z.; Pumera, M. Electrochemistry of Layered  
610 Metal Diborides. *Nanoscale* **2018**, *10*, 11544–11552.
- 611 (16) Suehara, S.; Aizawa, T.; Sasaki, T. Graphenelike Surface Boron Layer: Structural  
612 Phases on Transition-metal Diborides (0001). *Phys. Rev. B* **2010**, *81*, 085423.
- 613 (17) Qin, N.; Liu, S.-Y.; Li, Z.; Zhao, H.; Wang, S. First-principles Studies for the Stability  
614 of a Graphene-like Boron Layer on CrB<sub>2</sub> (0001) and MoB<sub>2</sub>(0001). *J. Phys.: Condens.*  
615 *Matter* **2011**, *23*, 225501.
- 616 (18) Liu, Y.; Penev, E. S.; Yakobson, B. I. Probing the Synthesis of Two-Dimensional Boron  
617 by First-Principles Computations. *Angew. Chem.* **2013**, *52*, 3156–3159.
- 618 (19) Zhao, H.; Qin, N. The Stability Boundary of Group-III Transition Metal Diboride ScB<sub>2</sub>  
619 (0001) Surfaces. *Appl. Surf. Sci.* **2012**, *258*, 3328 – 3330.
- 620 (20) Han, Y.; Dai, Y.; Shu, D.; Wang, J.; Sun, B. First-principles Study of TiB<sub>2</sub> (0001)  
621 Surfaces. *J. Condens. Matter Phys.* **2006**, *18*, 4197–4205.

- 622 (21) Wang, Y.; Michel, K.; Zhang, Y.; Wolverton, C. Thermodynamic Stability of Transition  
623 Metals on the Mg-terminated MgB<sub>2</sub> (0001) Surface and Their Effects on Hydrogen  
624 Dissociation and Diffusion. *Phys. Rev. B* **2015**, *91*, 155431.
- 625 (22) Prudilová, B.; Otyepková, E.; Fanfrlík, J.; Hnyk, D.; Holub, J.; Petr, M.; Filip, J.;  
626 Čépe, K.; Lazar, P.; Otyepka, M. Surface Termination of MgB<sub>2</sub> Unveiled by a Combi-  
627 nation of Adsorption Experiments and Theoretical Calculations. *Phys. Chem. Chem.*  
628 *Phys.* **2019**, *21*, 7313–7320.
- 629 (23) Callcott, T. A.; Lin, L.; Woods, G. T.; Zhang, G. P.; Thompson, J. R.; Paranthaman,  
630 M.; Ederer, D. L. Soft-x-ray Spectroscopy Measurements of the *p*-like Density  
631 of States of B in MgB<sub>2</sub> and Evidence for Surface Boron Oxides on Exposed Surfaces.  
632 *Phys. Rev. B* **2001**, *64*, 132504.
- 633 (24) Ray, K. G.; Klebanoff, L. E.; Lee, J. R. I.; Stavila, V.; Heo, T. W.; Shea, P.; Baker, A. A.;  
634 Kang, S.; Bagge-Hansen, M.; Liu, Y.-S.; White, J. L.; Wood, B. C. Elucidating the  
635 Mechanism of MgB<sub>2</sub> Initial Hydrogenation via a Combined Experimental–theoretical  
636 Study. *Phys. Chem. Chem. Phys.* **2017**, *19*, 22646–22658.
- 637 (25) Li, H.; Wen, P.; Li, Q.; Dun, C.; Xing, J.; Lu, C.; Adhikari, S.; Jiang, L.; Carroll, D. L.;  
638 Geyer, S. M. Earth-Abundant Iron Diboride (FeB<sub>2</sub>) Nanoparticles as Highly Active  
639 Bifunctional Electrocatalysts for Overall Water Splitting. *Adv. Energy Mater.* **2017**, *7*,  
640 1700513.
- 641 (26) Kim, C.-E.; Ray, K. G.; Bahr, D. F.; Lordi, V. Electronic Structure and Surface Prop-  
642 erties of MgB<sub>2</sub> (0001) upon Oxygen Adsorption. *Phys. Rev. B* **2018**, *97*, 195416.
- 643 (27) Ogitsu, T.; Gygi, F.; Reed, J.; Motome, Y.; Schwegler, E.; Galli, G. Imperfect Crystal  
644 and Unusual Semiconductor: Boron, a Frustrated Element. *J Am. Chem. Soc.* **2009**,  
645 *131*, 1903–1909, PMID: 19191703.

- 646 (28) Ogitsu, T.; Gygi, F. m. c.; Reed, J.; Udagawa, M.; Motome, Y.; Schwegler, E.; Galli, G.  
647 Geometrical Frustration in an Elemental Solid: An Ising Model to Explain the Defect  
648 Structure of  $\beta$ -rhombohedral Boron. *Phys. Rev. B* **2010**, *81*, 020102.
- 649 (29) Gunda, H.; Das, S. K.; Jasuja, K. Simple, Green, and High-Yield Production of Boron-  
650 Based Nanostructures with Diverse Morphologies by Dissolution and Recrystallization  
651 of Layered Magnesium Diboride Crystals in Water. *ChemPhysChem* **2018**, *19*, 880–891.
- 652 (30) Gunda, H.; Ghoroi, C.; Jasuja, K. Layered magnesium diboride and its derivatives as  
653 potential catalytic and energetic additives for tuning the exothermicity of ammonium  
654 perchlorate. *Thermochim. Acta* **2020**, *690*, 178674.
- 655 (31) Niehus, H.; Heiland, W.; Taglauer, E. Low-energy ion scattering at surfaces. *Surf. Sci.*  
656 *Rep.* **1993**, *17*, 213–303.
- 657 (32) Mikhailov, S.; van den Oetelaar, L.; Brongersma, H. Strong matrix effect in low-energy  
658 He<sup>+</sup> ion scattering from carbon. *Nuclear Instruments and Methods in Physics Research*  
659 *Section B: Beam Interactions with Materials and Atoms* **1994**, *93*, 210–214.
- 660 (33) Liu, Y.-S.; Klebanoff, L.; Wijeratne, P.; Cowgill, D.; Stavila, V.; Heo, T.; Kang, S.;  
661 Baker, A.; Lee, J.; Mattox, T.; Ray, K.; Sugar, J.; Wood, B. Investigating Possible  
662 Kinetic Limitations to MgB<sub>2</sub> Hydrogenation. *Int. J. Hydrogen Energy* **2019**, *44*, 31239  
663 – 31256.
- 664 (34) Wang, Y.; Michel, K.; Wolverton, C. Hydrogen Diffusion in Bulk MgB<sub>2</sub>. *Scr. Mater.*  
665 **2016**, *117*, 86 – 91.
- 666 (35) Wood, B. C.; Heo, T. W.; Kang, S.; Wan, L. F.; Li, S. Beyond Idealized Models of  
667 Nanoscale Metal Hydrides for Hydrogen Storage. *Ind. Eng. Chem. Res.* **0**, *0*, null.
- 668 (36) James, A. L.; Jasuja, K. Chelation assisted exfoliation of layered borides towards syn-  
669 thesizing boron based nanosheets. *RSC Adv.* **2017**, *7*, 1905–1914.

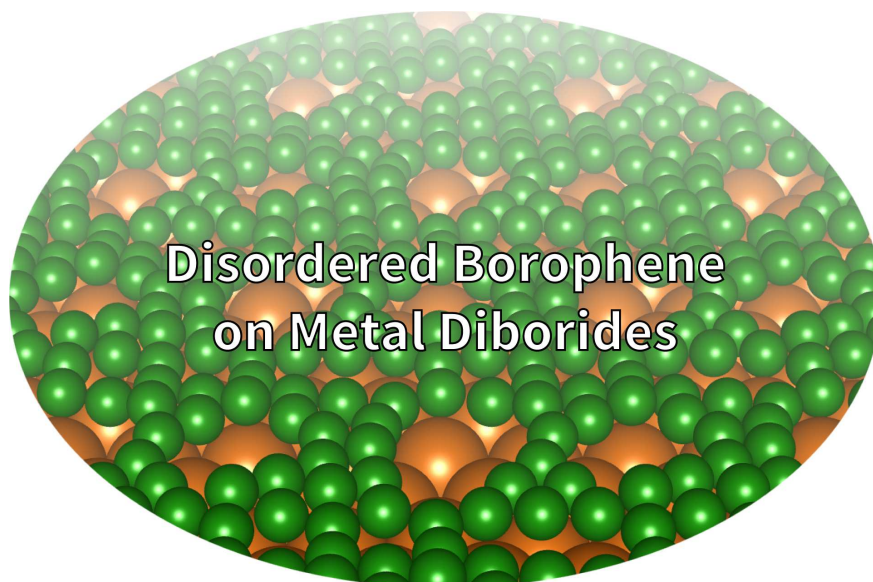
- 670 (37) Patidar, R.; Gunda, H.; Varma, A. K.; Gawas, R.; Das, S. K.; Jasuja, K. Co-solvent  
671 exfoliation of layered titanium diboride into few-layer-thick nanosheets. *Ceram. Int.*  
672 **2020**, *46*, 28324–28331.
- 673 (38) Hu, X.; Guo, S.; Zhang, S.; Guo, X.; Li, Y.; Huang, S.; Zhang, K.; Zhu, J. Two-  
674 dimensional Transition Metal Diborides: Promising Dirac Electrocatalysts with Large  
675 Reaction Regions toward Efficient N<sub>2</sub> Fixation. *J. Mater. Chem. A* **2019**, *7*, 25887–  
676 25893.
- 677 (39) Gild, J.; Zhang, Y.; Harrington, T.; Jiang, S.; Hu, T.; Quinn, M. C.; Mellor, W. M.;  
678 Zhou, N.; Vecchio, K.; Luo, J. High-Entropy Metal Diborides: A New Class of High-  
679 Entropy Materials and a New Type of Ultrahigh Temperature Ceramics. *Sci. Rep.*  
680 **2016**, *6*, 37946.
- 681 (40) James, A. L.; Khandelwal, S.; Dutta, A.; Jasuja, K. Boron based nanosheets as reducing  
682 templates in aqueous solutions: towards novel nanohybrids with gold nanoparticles and  
683 graphene. *Nanoscale* **2018**, *10*, 20514–20518.
- 684 (41) Gunda, H.; Klebanoff, L. E.; Sharma, P. A.; Varma, A. K.; Dolia, V.; Jasuja, K.;  
685 Stavila, V. Progress, Challenges, and Opportunities in the Synthesis, Characteriza-  
686 tion, and Application of Metal-Boride-Derived Two-Dimensional Nanostructures. *ACS*  
687 *Mater. Lett.* **0**, *0*, 535–556.
- 688 (42) James, A. L.; Lenka, M.; Pandey, N.; Ojha, A.; Kumar, A.; Saraswat, R.; Thareja, P.;  
689 Krishnan, V.; Jasuja, K. Processable dispersions of photocatalytically active nanosheets  
690 derived from titanium diboride: self assembly into hydrogels and paper-like macrostruc-  
691 tures. *Nanoscale* **2020**, *12*, 17121–17131.
- 692 (43) Kresse, G.; Furthmüller, J. Efficient Iterative Schemes for ab initio Total-energy Cal-  
693 culations Using a Plane-wave Basis Set. *Phys. Rev. B* **1996**, *54*, 11169–11186.
- 694 (44) Blöchl, P. E. Projector Augmented-wave Method. *Phys. Rev. B* **1994**, *50*, 17953–17979.

- 695 (45) Kresse, G.; Joubert, D. From Ultrasoft Pseudopotentials to the Projector Augmented-  
696 wave Method. *Phys. Rev. B* **1999**, *59*, 1758–1775.
- 697 (46) Perdew, J. P.; Burke, K.; Ernzerhof, M. Generalized Gradient Approximation Made  
698 Simple. *Phys. Rev. Lett.* **1996**, *77*, 3865–3868.
- 699 (47) Jain, A.; Ong, S. P.; Hautier, G.; Chen, W.; Richards, W. D.; Dacek, S.; Cholia, S.;  
700 Gunter, D.; Skinner, D.; Ceder, G.; Persson, K. A. Commentary: The Materials Project:  
701 A materials genome approach to accelerating materials innovation. *APL Mater.* **2013**,  
702 *1*, 011002.
- 703 (48) Hart, G. L.; Nelson, L. J.; Forcade, R. W. Generating Derivative Structures at a Fixed  
704 Concentration. *Comp. Mat. Sci.* **2012**, *59*, 101 – 107.
- 705 (49) Ong, S. P.; Richards, W. D.; Jain, A.; Hautier, G.; Kocher, M.; Cholia, S.; Gunter, D.;  
706 Chevrier, V. L.; Persson, K. A.; Ceder, G. Python Materials Genomics (pymatgen): A  
707 robust, open-source python library for materials analysis. *Comp. Mat. Sci.* **2013**, *68*,  
708 314 – 319.
- 709 (50) Larsen, A. H. et al. The Atomic Simulation Environment: a Python Library for Working  
710 with Atoms. *J. Phys. Condens. Matter.* **2017**, *29*, 273002.
- 711 (51) Otani, M.; Sugino, O. First-principles Calculations of Charged Surfaces and Interfaces:  
712 A Plane-wave Nonrepeated Slab Approach. *Phys. Rev. B* **2006**, *73*, 115407.
- 713 (52) Giannozzi, P. et al. Advanced capabilities for materials modelling with Quantum  
714 ESPRESSO. *J. Condens. Matter Phys.* **2017**, *29*, 465901.
- 715 (53) Henkelman, G.; Uberuaga, B. P.; Jónsson, H. A Climbing Image Nudged Elastic Band  
716 Method for Finding Saddle Points and Minimum Energy Paths. *J. Chem. Phys.* **2000**,  
717 *113*, 9901–9904.

- 718 (54) Henkelman, G.; Jónsson, H. Improved Tangent Estimate in the Nudged Elastic Band  
719 Method for Finding Minimum Energy Paths and Saddle Points. *J. Chem. Phys.* **2000**,  
720 *113*, 9978–9985.
- 721 (55) Henkelman, G.; Arnaldsson, A.; Jónsson, H. A Fast and Robust Algorithm for Bader  
722 Decomposition of Charge Density. *Comput. Mater. Sci.* **2006**, *36*, 354 – 360.
- 723 (56) Sanville, E.; Kenny, S. D.; Smith, R.; Henkelman, G. Improved Grid-based Algorithm  
724 for Bader Charge Allocation. *J. Comput. Chem.* **2007**, *28*, 899–908.
- 725 (57) Tang, W.; Sanville, E.; Henkelman, G. A Grid-based Bader Analysis Algorithm without  
726 Lattice Bias. *J. Phys.: Condens. Matter* **2009**, *21*, 084204.
- 727 (58) Laio, A.; Rodriguez-Fortea, A.; Gervasio, F. L.; Ceccarelli, M.; Parrinello, M. Assessing  
728 the accuracy of metadynamics. *J. Phys. Chem. B* **2005**, *109*, 6714–6721.
- 729 (59) Li, S.; Zheng, Y.; Gao, F.; Szanyi, J.; Schneider, W. F. Experimental and Computa-  
730 tional Interrogation of Fast SCR Mechanism and Active Sites on H-Form SSZ-13. *ACS*  
731 *Catal.* **2017**, *7*, 5087–5096.
- 732 (60) Wales, D. J.; Scheraga, H. A. Global Optimization of Clusters, Crystals, and  
733 Biomolecules. *Science* **1999**, *285*, 1368–1372.
- 734 (61) Wales, D. J.; Doye, J. P. K. Global Optimization by Basin-Hopping and the Lowest  
735 Energy Structures of Lennard-Jones Clusters Containing up to 110 Atoms. *J. Phys.*  
736 *Chem. A* **1997**, *101*, 5111–5116.
- 737 (62) Massobrio, C., Du, J., Bernasconi, M., Salmon, P. S., Eds. *Molecular Dynamics Simula-*  
738 *tions of Disordered Materials: From Network Glasses to Phase-Change Memory Alloys*;  
739 Springer Series in Materials Science; Springer International Publishing, 2015.
- 740 (63) Bastasz, R.; Whaley, J. A.; Lograsso, T. A.; Jenks, C. J. Hydrogen interactions with  
741 quasicrystalline Al–Pd–Mn surfaces. *Philosophical Magazine* **2006**, *86*, 855–862.

742 (64) Wong, C.-S.; Whaley, J. A.; Bergstrom, Z. J.; Wirth, B. D.; Kolasinski, R. D. Exper-  
743 imental characterization of hydrogen adsorption sites for H/W(111) using low energy  
744 ion scattering. *Phys. Rev. B* **2019**, *100*, 245405.

## 745 5 TOC Graphic



## Supplementary Files

This is a list of supplementary files associated with this preprint. Click to download.

- [SI.pdf](#)